



CrossMark
 click for updates

Cite this: *RSC Adv.*, 2016, 6, 65475

A study of CO₂/CO separation by sub-micron *b*-oriented MFI membranes

D. Korelskiy,* M. Grahn, P. Ye, M. Zhou and J. Hedlund

Separation of CO₂ and CO is of great importance for many industrial applications. Today, CO₂ is removed from CO mainly by adsorption or physical or chemical absorption systems that are energy-intensive and expensive. Membranes are listed among the most promising sustainable and energy-efficient alternatives for CO₂ separation. Here, we study CO₂/CO separation by novel sub-micron *b*-oriented MFI zeolite membranes in a temperature range of 258–303 K and at a feed pressure of 9 bar. Under all experimental conditions studied, the membranes were CO₂-selective and displayed high CO₂ permeance ranging from 17 000 to 23 000 gpu. With decreasing temperature, the CO₂/CO selectivity was increasing, reaching a maximum of 26 at 258 K. We also developed a mathematical model to describe the membrane process, and it indicated that the membrane separation performance was a result of selective adsorption of CO₂ on the polar zeolite. The heat of adsorption of CO₂ on the zeolite is more negative due to the high quadrupole moment and polarisability of the molecule as compared to CO. At the same time, diffusional coupling (correlation effects) at high adsorbed loadings was found to favour the overall CO₂/CO selectivity of the membranes by reducing the diffusivity of the lighter CO molecule in the ca. 0.55 nm pores in the zeolite. The model also indicated that the separation performance was limited by the mass transfer resistance in the support and concentration polarisation on the feed side of the membrane.

Received 4th June 2016
 Accepted 5th July 2016

DOI: 10.1039/c6ra14544b

www.rsc.org/advances

Introduction

CO is used for manufacture of a wide range of valuable chemicals, such as oxo-alcohols, phosgene (intermediate for polyurethane), methanol, acetic acid or various liquid hydrocarbon fuels *via* the Fischer-Tropsch process. CO itself is often produced by gasification (partial oxidation) of carbon-containing materials, *e.g.* coal, biomass, *etc.*, or steam reforming of natural gas. In addition to CO, the produced gas mixture, referred to as synthesis gas, contains H₂, CO₂ and minor impurities, *e.g.* N₂, H₂O, H₂S, *etc.* To utilise for the synthesis of chemicals, CO usually has to be purified, mainly from CO₂. For instance, the gas used for oxo-synthesis should contain ≤0.5% of CO₂.¹ Separation of CO and CO₂ is, however, challenging since the properties of the two gases are rather similar. Most of the currently available CO₂ separation methods rely on adsorption or absorption, *e.g.* pressure swing adsorption or amine scrubbing.² Despite certain advantages, the sorption-based separation systems are cumbersome, rather energy-intensive and require large capital investments.³ Moreover, the absorbents used today are often corrosive and may release hazardous substances into the environment.

Membranes are an appealing alternative to many common separation technologies, including adsorption, absorption and

cryogenic distillation. High efficiency, sustainability and low energy demand are defining characteristics of membrane-based separation methods. Moreover, membrane separation processes are simple and continuous, requiring a minimum of process equipment. For instance, we have recently demonstrated⁴ that only one module housing 10 m² of membrane area could replace an entire amine scrubbing system for separation of 300 ton CO₂ per day from synthesis gas. It is worth pointing out that membranes have been listed among the most promising CO₂ separation and capture technologies.³ The CO₂-selective membranes currently available on the market are polymeric membranes. These membranes can be manufactured in large quantities at fairly low costs. At the same time, large membrane areas are a necessity for a given separation task because the membranes have low permeability, often coupled with a fairly poor selectivity. For example, Polaris™ membranes have a CO₂ permeance of 100–300 gpu (1 gpu = 3.35 × 10⁻¹⁰ mol s⁻¹ m⁻² Pa⁻¹) and a CO₂/CO selectivity of 10–20 at a temperature ranging from 268 to 298 K.⁵ Even state-of-the-art CO₂-selective polymeric membranes display a CO₂ permeance of at most 1000 gpu.⁶ In addition, CO₂ has a detrimental effect on the membrane stability, especially at high concentrations (pressures), reducing the membrane performance and lifespan.³

Among inorganic CO₂-selective membranes, zeolite membranes are particularly attractive.⁷ These membranes have a well-defined pore system with pores ranging from 0.3 to 1.3

Chemical Technology, Luleå University of Technology, SE-97187 Luleå, Sweden.
 E-mail: danil.korelskiy@ltu.se



nm in size.⁸ Hence, zeolite membranes are microporous membranes. Due to the microporous structure, the separation mechanism by zeolite membranes can rely on molecular sieving (size exclusion), differences in adsorption or differences in diffusion between the separated components. Being highly porous and thin, zeolite membranes can exhibit much higher fluxes than polymeric membranes.⁹ Currently, zeolite films as thin as 100 nm can be prepared, displaying a high *n*-butane permeance up to *ca.* 4000 gpu.¹⁰ As a consequence, much lower membrane areas would suffice for a given separation task. In addition, the chemical and thermal stability of zeolite membranes is vastly superior to that of polymeric membranes.¹¹

In spite of the great interest in separation of the main components of synthesis gas, *i.e.* CO, H₂ and CO₂, the number of research reports on zeolite membranes for this separation is small.⁷ In particular, CO₂/CO membrane separation has scarcely been studied. Our research group¹³ has previously evaluated a sub-micron randomly oriented highly siliceous MFI zeolite membrane for the separation of an equimolar mixture of CO₂, H₂ and CO. The membrane was CO₂-selective with a high CO₂ permeance up to *ca.* 24 000 gpu. At a temperature of 277 K and a feed pressure of 9 bar, a CO₂/CO membrane selectivity of *ca.* 10 was reported. The highly siliceous MFI zeolite (also referred to as siliceous ZSM-5 with a unit cell represented by the

general chemical formula [Si₉₆O₁₉₂]-MFI)¹⁴ has a three-dimensional pore structure comprised of two types of intersecting pores, *viz.* tortuous and straight with an average pore diameter of *ca.* 0.55 nm.¹² The tortuous (sinusoidal) pores are running in the *a*-direction, whereas the straight pores are running in the *b*-direction, see Fig. 1. Molecules can also diffuse in the *c*-direction by alternating between the straight and sinusoidal pores. However, the diffusion in the *c*-direction is significantly slower than in the *a*- and *b*-directions.^{15,16} It has been shown^{14,17} that *b*-oriented MFI films may allow for somewhat faster transport of molecules, especially bulky molecules (*e.g.* xylenes) since the straight pores will be running along the film thickness. The *b*-orientation has therefore been considered preferable.

Recently, we¹⁸ have developed a sub-micron *b*-oriented MFI membrane employing a fluoride route (neutral pH) for the synthesis. The developed membranes displayed high CO₂/H₂ and CO₂/CO selectivities up to *ca.* 110 and 20, respectively. Here, we extend our previous work on CO₂/CO separation using sub-micron *b*-oriented MFI membranes by developing a model to elucidate the separation mechanism and describe the effect of the support and concentration polarisation on the membrane separation performance. In addition, the morphology of the membranes, especially the grain boundaries and grain size, was carefully studied by SEM. Permporometry data were used to estimate the width of the open grain boundaries and the grain size, and the findings were compared with the SEM data.

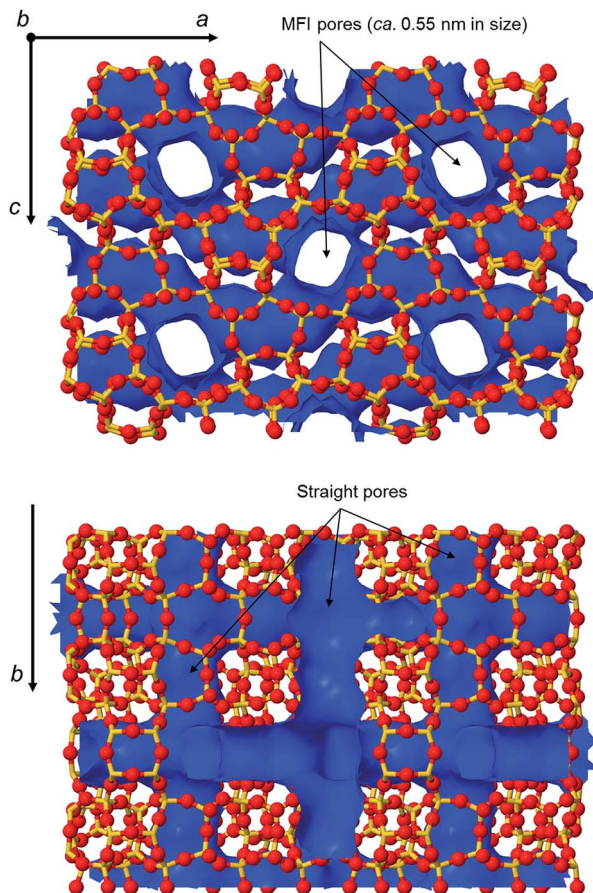


Fig. 1 Schematic representation of the MFI zeolite crystal structure¹² (the pore surface is in blue).

Experimental

Membrane synthesis

Sub-micron (*ca.* 0.5 μm) *b*-oriented MFI zeolite membranes were prepared as described in detail in our previous work.¹⁸ The membranes were supported on a commercial graded α -alumina disc (Fraunhofer IKTS, Germany) with a diameter of 25 mm. A brief summary of the membrane preparation procedure is given below. In the first step, the supports were seeded with plate-shaped MFI crystals with a size of 500 \times 450 \times 200 nm. The seed crystals were synthesised from a mixture containing tetraethyl orthosilicate (TEOS), tetrapropylammonium hydroxide (TPAOH) and water with a respective molar ratio of 1 : 0.2 : 100. The mixture was kept at 403 K for 9 h. In the second step, zeolite films were grown on the seeded supports by hydrothermal synthesis at 373 K for 48 h using a synthesis mixture with a molar composition of SiO₂ : 0.12TPAOH : 60H₂O : 0.12HF. After the synthesis, the membranes were rinsed with a 0.2 M ammonia solution and dried at 323 K overnight. The following day, the membranes were calcined at 773 K for 6 h at a heating rate of 0.2 K min⁻¹ and a cooling rate of 0.3 K min⁻¹.

Membrane characterisation

The morphology of the membranes was characterised by Scanning Electron Microscopy (SEM) using a Magellan 400 SEM (the FEI Company, The Netherlands). Cross-sections of the membranes were obtained by fracturing the membranes with



a pair of cutting pliers. No conductive coating was applied to the samples.

The quality of the membranes in terms of defects was evaluated by *n*-hexane/helium permoporometry¹⁹ as described in detail in our earlier work²⁰ and in brief here. The membranes were mounted in a stainless steel cell using graphite gaskets (Eriks, The Netherlands) for sealing. In order to remove any adsorbed compounds, the membranes were heated to 573 K at a heating rate of 1 K min⁻¹ and kept at this temperature for 6 h in a flow of pure helium (99.999%, AGA). The permoporometry experiment was performed at a temperature of 323 K, a total feed pressure of 2 bar and a total permeate pressure of 1 bar. The relative pressure of *n*-hexane (99%, Alfa Aesar) in the feed was increased in a step-wise manner from 0 to *ca.* 0.4. At each relative pressure, the system was allowed to equilibrate. In order to remove *n*-hexane from the permeate stream, a condenser kept at 233 K followed by a column packed with activated carbon were employed. A soap bubble flow meter was used to measure the *n*-hexane-free permeate volumetric flow rate. For each *n*-hexane relative pressure, a defect width was calculated by either the Horvath–Kawazoe equation (micropore-range defects) or the Kelvin equation complemented by the Harkins–Jura equation accounting for the thickness of the adsorbed layer (mesopore-range defects). For each defect interval, the average defect width was then calculated. Based on the average defect width, the average helium diffusivity in each defect interval was estimated using the gas-translational model. Knowing the diffusivity, the helium molar flux was further calculated from Fick's law. The area of defects was estimated as the ratio between helium molar flow and flux through the defects in that particular interval. In the final step, the relative area of defects was calculated by dividing the area of defects with the total membrane area. More details about the evaluation procedure of the permoporometry data can be found in our previous work.²⁰

In order to identify the type of defects detected by permoporometry, a geometrical model of the membrane microstructure was used. It is worth noting that this model is only a rough approximation of the microstructure. In the model, the grains were assumed to have a cuboid habit with a square cross-section with a width of *x*, see Fig. 2. It should be noted that the cuboid habit with a square cross-section was only assumed to simplify the calculation of the grain surface area from the permoporometry data. The grain width was assumed to be constant throughout the film thickness. The micropore defects with a weighted arithmetic average width of *d* were assumed to be evenly distributed between the grains, as shown in Fig. 2. Therefore, the relative area of micropore defects *a* can be calculated as

$$a = \frac{d(x + d + x)}{(x + d)^2} \quad (1)$$

Since *d* is much smaller than *x*, eqn (1) can be simplified to

$$a = \frac{2d}{x} \quad (2)$$

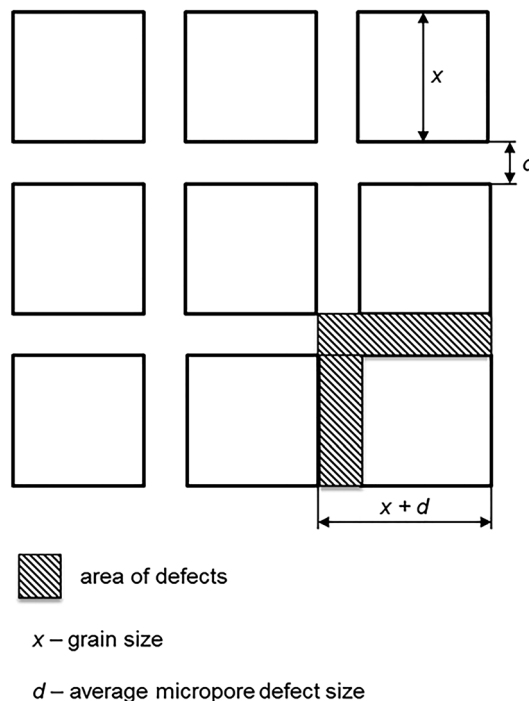


Fig. 2 A geometrical model of the membrane microstructure.

The relative area of micropore defects *a* can be estimated from permoporometry data obtained experimentally. Knowing the relative area, the grain size *x*, and hence the grain surface area, can then easily be calculated using eqn (2).

CO₂/CO separation experiments

Mixed-gas separation experiments were carried out using a 50/50 (v/v) mixture of CO₂ (99.999%, AGA) and CO (99.97%) at a total feed pressure of 9 bar and a total permeate pressure of 1 bar. The membrane was kept in the cell used for the permoporometry test. The experiments were carried out at a temperature ranging from 258 to 303 K. Prior to the experiments, the membrane was dried at 573 K for 6 h using a stream of pure helium (99.999%, AGA) to remove any adsorbed species. The volumetric flow rate of the permeate was measured with a drum-type gasmeter (TG Series, Ritter Apparatebau GmbH), and the composition of the permeate was analysed with a mass spectrometer (GAM 400, InProcess Instruments).

The flux of component *i*, *J_i* (mol s⁻¹ m⁻²), was estimated from the measured molar flow rate of the corresponding component through the membrane, *F_i* (mol s⁻¹) as

$$J_i = F_i/A, \quad (3)$$

where *A* is the membrane area (m²).

The permeance of component *i*, *Π_i* (mol s⁻¹ m⁻² Pa⁻¹), was calculated from the flux of the corresponding component through the membrane as

$$\Pi_i = J_i/\Delta P_i, \quad (4)$$



where ΔP_i (Pa) is the partial pressure difference of component i across the membrane. It should be noted that for gas permeation and separation, permeance is normally reported in gpu (gas permeation units), where 1 gpu is equal to $3.35 \times 10^{-10} \text{ mol s}^{-1} \text{ m}^{-2} \text{ Pa}^{-1}$.

The CO_2/CO membrane selectivity, $\alpha_{\text{CO}_2/\text{CO}}$, was estimated as

$$\alpha_{\text{CO}_2/\text{CO}} = \Pi_{\text{CO}_2}/\Pi_{\text{CO}} \quad (5)$$

Modelling

For composite membranes, as in this work, high flux may cause both concentration polarisation on the feed side and a pressure drop over the support. These effects may result in a decrease in the performance of the membrane, in terms of both flux and selectivity.^{21–23} To assess to what extent these effects may have influenced the separation performance of the membrane in the present work, a mathematical model was used. The model has been described in detail elsewhere^{21,23,24} and will only be described briefly below.

The effect of concentration polarisation may be evaluated by determining the concentration polarisation index (CPI) as

$$\text{CPI} = \exp(J_v/k_c) + \frac{n_p}{n_b} [1 - \exp(J_v/k_c)], \quad (6)$$

where n_b is the mole fraction in the gas bulk, k_c is the mass transfer coefficient, J_v is the volumetric flux and n_p is the mole fraction in the permeate. The mass transfer coefficient may be obtained from mass transfer correlations relating the Sherwood (Sh) number to the Reynolds (Re) and Schmidt (Sc) numbers. Perdana *et al.*²⁵ have reported a correlation for mass transfer in a Wicke–Kallenbach cell, which is used in the present work.

$$\text{Sh} = 2.83 + 2.24\text{Re}^{0.58}\text{Sc}^{0.33} \left(\frac{w}{D_C} \right)^{1.30}, \quad (7)$$

where w is the compartment height, *i.e.* the thickness of the gas film on the feed side of the membrane and D_C is the diameter of the membrane inside the gaskets, for more details see Perdana *et al.*²⁵ The mass transfer coefficient was finally retrieved from the Sherwood number:

$$\text{Sh} = \frac{k_c d_h}{D}, \quad (8)$$

where d_h is the hydraulic diameter of the cell and D is the gas phase diffusivity of CO_2 .

The pressure drop across each layer of the support was determined using procedures described in detail elsewhere.^{21,26–28} The transport through the 3 mm thick base layer with 3 μm pores was assumed to occur *via* viscous flow, whereas transport through the 30 μm thick top layer was assumed to occur *via* a combination of viscous flow and Knudsen diffusion. Effective permeabilities and Knudsen transport coefficients for each of the support layer have been reported in our previous work.²¹

Gas phase diffusivities and viscosities were adjusted to the desired temperature using the $D_i \propto T^{3/2}$ relationship and Sutherland's equation,²⁹ respectively. The viscosities of the

mixtures were calculated as molar fraction weighted averages. The ideal adsorbed solution theory (IAST)³⁰ was used to estimate adsorbed loadings on the feed side of the membrane during the separation experiment. Saturation loadings, Langmuir affinity coefficients and adsorption enthalpies were taken from the literature.^{31–34}

Results and discussion

Membrane characterisation

Fig. 3 shows cross-sectional and top-view SEM images of an as-synthesised membrane. It is evident that the MFI crystals comprising the film were mainly *b*-oriented. The MFI film was even and continuous, and the crystal length in the *b*-direction, *i.e.* the film thickness, was *ca.* 0.5 μm . The crystals composing the dense part of the film appear to be well-intergrown with

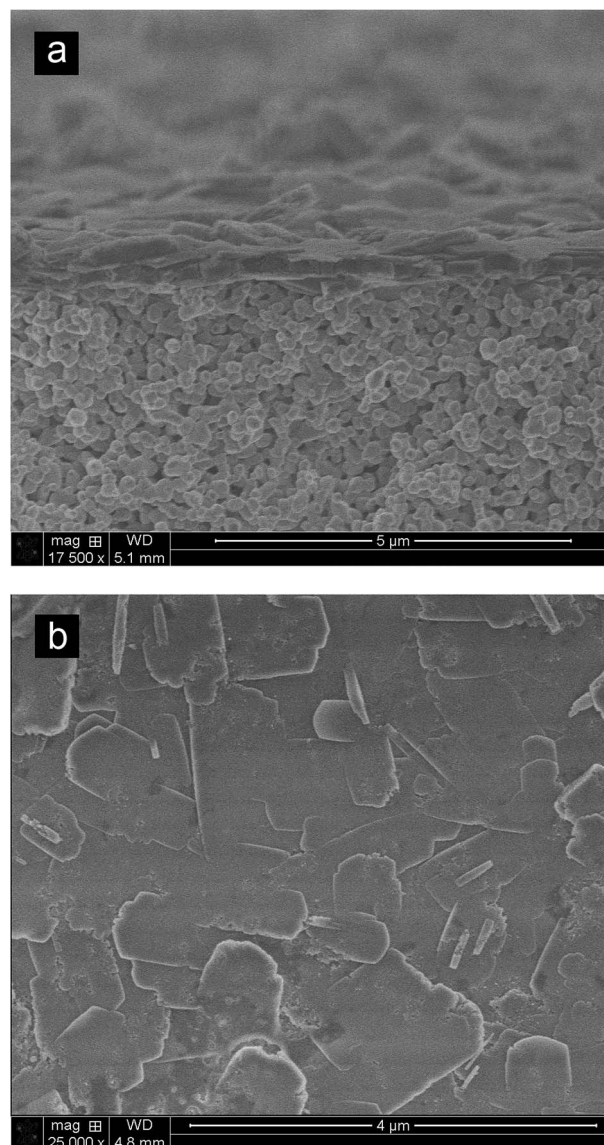


Fig. 3 Cross-sectional (a) and top-view (b) SEM images of an as-synthesised membrane.



a smooth top surface. However, some of the crystals were sticking out of the dense part of the film, displaying a typical rounded boat shape.³⁵ The in-plane dimensions of the crystals composing the dense part of the film were found to vary considerably. However, the maximum lengths along the *a*-axis and *c*-axis were *ca.* 0.5 μm and 2 μm , respectively. Defects in the form of cracks and pinholes, which are normally larger than 5 nm, were not detected by SEM. The absence of such defects indicates high quality of the membrane. In Fig. 3a, part of the top layer of the support can also be observed. The grain size of the support is about 150 nm and the pore size is about 100 nm. No growth of the zeolite into the support, often referred to as invasion,³⁶ could be detected, which is desired as the invasion would reduce the permeability of the support. The absence of the invasion can most likely be attributed to the good seeding, resulting in a dense seed layer protecting the support. The *b*-oriented MFI phase comprising as-synthesised membranes was corroborated by X-ray diffraction (XRD), and the data were reported in our previous work.¹⁸

Table 1 shows the helium permeance through the synthesised membrane measured at each relative pressure of *n*-hexane in the permoporometry experiment. The table also shows the relative areas of defects estimated for each defect interval. In the permoporometry experiment, the initial measuring point is recorded at a relative pressure of *n*-hexane of 0. The helium permeance at this point denotes the combined permeance through zeolite pores and defects. For this membrane, the initial helium permeance was high amounting to *ca.* 20 000 gpu, indicating that the zeolite pores are open and permeable. With increasing relative pressure of *n*-hexane, first MFI pores and then defects were blocked by *n*-hexane causing the helium permeance to decrease. The total relative area of defects in the membrane was very small, scarcely above 0.1% of the total membrane area, indicating a very high quality of the membrane. The few detected defects were essentially only micropore defects, accounting for *ca.* 99.6% of all defects. Virtually no mesopore defects were detected by permoporometry, which is consistent with the SEM observations.

In our previous work, we showed that the micropore defects detected by permoporometry in our randomly oriented high-flux MFI membranes were open grain boundaries. In order to identify whether the detected micropore defects in the *b*-

oriented MFI membranes prepared in the present work were as well open grain boundaries, we used a rough geometrical model of the membrane microstructure described in the Experimental. The average width of micropore defects *d* was estimated from the permoporometry data as a weighted arithmetic mean to be 0.79 nm. For this particular membrane, the relative area of micropore defects *a* was *ca.* 0.13% yielding a grain size *x* of *ca.* 1.2 μm (see eqn (2)), and consequently a square grain with a surface area of *ca.* 1.4 μm^2 . In spite of the great simplicity of the model, the grain size estimated from the permoporometry data was in excellent agreement with the grain sizes observed by SEM, *i.e.* the maximum lengths along the *a*- and *c*-axis of *ca.* 0.5 and 2 μm corresponding to a square grain with a surface area of 1 μm^2 . The latter indicates that the micropore defects detected by permoporometry in the prepared membrane should mainly be open grain boundaries.

CO₂/CO separation experiments

Fig. 4 shows mixed-gas permeances of CO₂ and CO as a function of temperature. High mixed-gas permeances up to 23 000 gpu were observed, and the permeance of CO₂ was higher than that of CO in the entire temperature range. With decreasing temperature, the permeances of both CO₂ and CO were decreasing. Bakker *et al.*³⁷ studied temperature dependence of pure-gas permeation of various gases through MFI membranes. It was found that the diffusion of CO₂ and CO in the membranes was activated surface diffusion, for which the diffusivity is increasing with increasing temperature, following an Arrhenius-type expression. The same type of temperature dependence was also found by Kärger *et al.*,³⁸ who studied the intracrystalline self-diffusion of CO₂ and CO in MFI zeolite by NMR. Thus, the decrease in permeance with decreasing temperature observed in the present work should emanate from the decrease in the diffusivities. It should be noted, however, that even at the lowest studied temperature of 258 K the permeance of CO₂ was as high as *ca.* 17 000 gpu.

Fig. 5 shows CO₂/CO mixed-gas membrane selectivity as a function of temperature. At the highest studied temperature

Table 1 Permoporometry data for the synthesised membrane

P/P_0	He permeance (1000 gpu)	Defect interval (nm)	Relative area of defects ^a (%)
0	20	—	—
2.3×10^{-4}	0.52	0.71–0.74	5.9×10^{-2}
3.7×10^{-4}	0.35	0.74–0.81	4.3×10^{-2}
1.1×10^{-3}	0.20	0.81–1.05	2.9×10^{-2}
1.1×10^{-2}	0.035	1.05–1.80	1.1×10^{-3}
1.2×10^{-1}	0.022	1.80–4.41	9.2×10^{-5}
3.7×10^{-1}	0.019	>4.41	4.6×10^{-4}
		Total	1.3×10^{-1}

^a Area of defects per total membrane area.

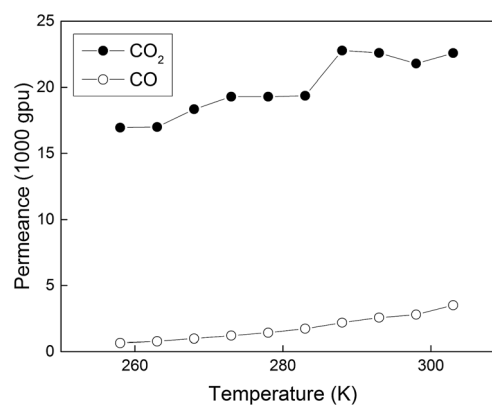


Fig. 4 CO₂ and CO permeances measured in the temperature range of 258–303 K at a feed pressure of 9 bar and a permeate pressure of 1 bar.



of 303 K, the CO₂/CO selectivity was *ca.* 6, and it was increasing with decreasing temperature, reaching a maximum of 26 at the lowest studied temperature of 258 K. Since the size of both CO₂ (0.33 nm) and CO (0.38 nm)³⁷ is smaller than the MFI pore size (0.55 nm), the separation mechanism should rely on the differences in either adsorption or diffusion for the two molecules, and not the molecular sieving. To further elucidate the findings, a modelling work was carried out, and the results will be discussed below.

Table 2 reports the CO₂ and CO fluxes, and the concentration of CO₂ and CO in the permeate stream. The observed CO₂ flux was very high, *i.e.* 320–440 kg m⁻² h⁻¹, in the entire temperature range. The high CO₂ flux is most likely a result of the very low thickness of the zeolite film, strong CO₂ adsorption and high CO₂ diffusivity in the zeolite pores, and a relatively high CO₂ partial pressure difference of 3.5 bar across the membrane.

In general, performance of supported zeolite membranes is defined by the properties of the active zeolite film and the support. If the thickness of the film is high (*e.g.* a few microns), the effect of the support on the membrane performance can be neglected since essentially all mass transfer resistance will

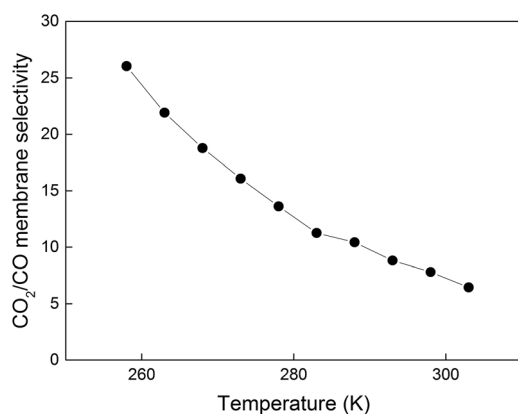


Fig. 5 CO₂/CO membrane selectivity determined in the temperature range of 258–303 K at a feed pressure of 9 bar and a permeate pressure of 1 bar.

Table 2 CO₂ and CO fluxes and permeate concentration observed in the present work

T (K)	Flux (kg h ⁻¹ m ⁻²)		Permeate concentration (mol%)	
	CO ₂	CO	CO ₂	CO
303	438	51	84.75	15.63
298	420	41	86.63	13.33
293	434	38	87.90	12.05
288	436	32	89.12	10.40
283	370	26	90.15	9.80
278	367	21	91.70	8.30
273	366	18	92.80	7.15
268	347	15	93.75	6.22
263	321	12	94.60	5.40
258	319	10	95.35	4.60

occur over the zeolite film. In other words, both the overall selectivity and flux of such a membrane will be defined by the properties of the film, which is preferable. However, the high film thickness results in very low flux,⁷ making the membrane impractical. In contrast, if the film thickness is low (*i.e.* below 1 μm), high fluxes, sufficient for a practical application, can be achieved, but the membrane performance may be influenced by the support, as its contribution to the overall mass transfer becomes significant. Roughly speaking, the lower the film thickness, the stronger the support may influence the membrane performance. The effect of the support can also be enhanced if the separated components are small, highly permeable molecules, such as CO₂ and CO, as their transport through the film will be even faster. Since the support is normally non-selective or sometimes adversely selective, its contribution to the mass transfer will reduce the separation performance of the membrane. Hence, the effect of the support on the performance of high-flux membranes should be taken into account. In our previous works,^{21–23} we showed that the pressure drop over the support adversely affected the performance of our high-flux membranes for liquid separation of alcohols and water, and gas separation of helium and nitrogen at cryogenic temperature. It is therefore important to study the effect of the support on CO₂/CO separation reported in the present work. In addition, high-flux membranes may suffer from concentration polarisation on the feed side, reducing the driving force over the film, and therefore selectivity and flux.²³ In the present work, we have studied the effects of these two phenomena for three different temperatures, *viz.* 303, 278 and 258 K. The selected points represent high, medium and low flux, respectively. Table 3 shows the results of the evaluation. The relative pressure drop over the support, Δ*P*, (*i.e.* pressure drop over the support/pressure drop over the whole composite membrane) was estimated to be 33%, 27% and 21% at 303, 278 and 258 K, respectively. These values are consistent with our previous findings for high-flux MFI zeolite membranes,^{21–23} indicating that the support adversely affected the performance of the membrane. Most of the resistance was found to be in the thin top layer of the support having 100 nm pores. Therefore, in order to improve the membrane separation performance, the negative effect of the support should be eliminated or at least minimised. One feasible way of minimising this effect would be to reduce the thickness of the top layer from 30 to, *e.g.* 5–10 μm.²⁴ The concentration polarisation index was determined to be 0.83, 0.87 and 0.90 at 303, 278 and 258 K, indicating that concentration polarisation reduced the performance of the

Table 3 Relative pressure drop over the support, concentration polarisation index (CPI), permselectivity, and adsorption and diffusional selectivity for the zeolite film estimated for three different temperatures

T (K)	Δ <i>P</i> (%)	CPI	α _{perm,film}	α _{ads}	α _{diff}
303	33	0.83	15	18	0.82
278	27	0.87	24	30	0.83
258	21	0.90	41	46	0.89



membrane, especially at the higher temperatures, where the flux was higher. In order to minimise the concentration polarisation effect and improve the membrane performance, higher feed flow rates would be required. Additionally, turbulence generating internals in the membrane cell could be used to improve the mass transfer on the feed side. It is also worth noting that if the film thickness were even lower, the negative effect of the support and concentration polarisation on the separation performance would be even higher, and it would thus be even more important to minimise these effects.

The permselectivities for the zeolite film after correcting for concentration polarisation and pressure drop over the support, $\alpha_{\text{perm, film}}$, were *ca.* 15, 24 and 41 at 303, 278 and 258 K, respectively. These values differ from the overall selectivities, *ca.* 6, 14 and 26, measured at the same temperatures (see Fig. 5). It is therefore evident that the membrane selectivity was significantly reduced by concentration polarisation and pressure drop over the support.

To better understand the experimental findings, we estimated the adsorption selectivity on the feed side of the membrane using the IAST, after removing the effect of the support and concentration polarisation, see Table 3. The CO₂/CO adsorption α_{ads} selectivity was increasing with decreasing temperature. This is expected because the heat of adsorption of CO₂ ($-24.1 \text{ kJ mol}^{-1}$) is more negative than that of CO ($-17.9 \text{ kJ mol}^{-1}$) due to the high quadrupole moment and polarisability of the CO₂ molecule as compared to CO.³² This also shows that the adsorption of CO₂ is stronger than the adsorption of CO. Moreover, the estimated adsorption selectivities were very similar to the permselectivities. The latter fact indicates that the membrane selectivity to CO₂ should mainly be ascribed to the stronger adsorption of CO₂ in the zeolite film. It should also be noted that the adsorption selectivity can probably be increased by increasing the polarity of the zeolite,³⁹ *i.e.* by decreasing the Si/Al ratio, resulting in even higher membrane selectivity to CO₂. Further, the permselectivity for zeolite membrane may be expressed as the product of the adsorption and diffusional selectivities:

$$\alpha_{\text{perm}} = \alpha_{\text{ads}} \times \alpha_{\text{diff}} \quad (9)$$

The diffusional selectivities may therefore be retrieved from the experimental data shown in Table 3. The diffusional selectivity only varies marginally, from 0.82 at the highest temperature to 0.89 at the lowest temperature. Only a few reports exist on transport of CO through MFI membranes, however Bakker *et al.*³⁷ have determined pure-gas diffusivities and activation energies of diffusion of CO₂ and CO in silicalite-1 from pure-gas membrane permeation data. For CO₂ and CO, they reported pure-gas diffusivities of 0.7×10^{-8} and $0.9 \times 10^{-8} \text{ m}^2 \text{ s}^{-1}$ and activation energies of diffusion of 9.6 and 7.1 kJ mol^{-1} , respectively. Noticeably, the ratio of the pure-gas diffusivities ($D_{\text{CO}_2}/D_{\text{CO}}$) yields 0.78, which is strikingly close to the diffusional selectivity of *ca.* 0.82 that we obtain in the present work at the higher temperatures. As the activation energy of diffusion for CO₂ is larger than that for CO, the diffusivity of CO₂ should decrease faster than that of CO with decreasing temperature. Consequently, the ratio of pure-gas diffusivities should also

decrease with decreasing temperature, *e.g.* by 19% for a temperature decrease from 299 to 248 K. However, our diffusional selectivity was slightly increasing with decreasing temperature, from *ca.* 0.82 to 0.89. We ascribe this to increased diffusional coupling (correlation effects) at reduced temperatures.³⁹ As the adsorbed loading of CO₂ increases, it becomes more effective in slowing down the diffusion of CO (the faster diffusing species), thereby leading to a slight increase in the diffusional selectivity with decreasing temperature. It is also worth noting that since the kinetic diameter of CO (0.38 nm) is larger than that of CO₂ (0.33 nm), the overall CO₂/CO selectivity can probably be increased further by using a smaller-pore zeolite, *e.g.* CHA zeolite, due to the additional molecular sieving effect favouring the permeation of CO₂. It would thus be interesting to develop high-flux CHA zeolite membranes for this separation.

To conclude, the adsorption selectivity was shown to be the dominating factor for the permselectivity observed in this work. In addition, at the high adsorbed loadings obtained at the lower temperatures, diffusional correlation effects also favour the overall CO₂/CO selectivity, by keeping the diffusional selectivity up (closer to unity).

Conclusions

Sub-micron *b*-oriented high-flux MFI zeolite membranes were prepared and carefully characterised by permoporometry and SEM. By comparing the permoporometry and SEM data, the micropore defects detected in the membranes by permoporometry were found to be open grain boundaries. The membranes were then evaluated for CO₂/CO separation at a temperature ranging from 258 to 303 K, a feed pressure of 9 bar and a permeate pressure of 1 bar. The membranes were CO₂-selective in the entire temperature range. The highest CO₂/CO selectivity of 26 was observed at the lowest studied temperature of 258 K. The selectivity of the membrane to CO₂ was attributed to the stronger CO₂ adsorption, which was supported by a mathematical model based on IAST. The adsorption selectivity, and hence the overall CO₂ selectivity can probably be increased further by increasing the polarity of the zeolite. It was also found that diffusional coupling (correlation effects) at high adsorbed loadings resulted in a slight increase of the diffusional selectivity, keeping it closer to unity. In addition, the model indicated that the separation performance of the membrane was reduced by the pressure drop across the support and concentration polarisation on the feed side. Hence, in order to improve the separation performance, these effects should be minimised by, for instance, reducing the thickness of the support and increasing the feed flow rates. Without these effects, a CO₂/CO selectivity of 41 would be achieved at the lowest studied temperature of 258 K.

Acknowledgements

Bio4Energy is gratefully acknowledged for financially supporting this work.



Notes and references

- 1 C. Higman and M. v. d. Burgt, *Gasification*, Gulf Professional Pub./Elsevier Science, Amsterdam, Boston, 2nd edn, 2008.
- 2 X. Y. Chen, H. Vinh-Thang, A. A. Ramirez, D. Rodrigue and S. Kaliaguine, *RSC Adv.*, 2015, **5**, 24399–24448.
- 3 S. D. Kenarsari, D. Yang, G. Jiang, S. Zhang, J. Wang, A. G. Russell, Q. Wei and M. Fan, *RSC Adv.*, 2013, **3**, 22739–22773.
- 4 D. Korelskiy, P. Ye, S. Fouladvand, S. Karimi, E. Sjöberg and J. Hedlund, *J. Mater. Chem. A*, 2015, **3**, 12500–12506.
- 5 H. Lin, Z. He, Z. Sun, J. Vu, A. Ng, M. Mohammed, J. Kniep, T. C. Merkel, T. Wu and R. C. Lambrecht, *J. Membr. Sci.*, 2014, **457**, 149–161.
- 6 R. W. Baker and B. T. Low, *Macromolecules*, 2014, **47**, 6999–7013.
- 7 M. Pera-Titus, *Chem. Rev.*, 2013, **114**, 1413–1492.
- 8 J. Caro and M. Noack, *Microporous Mesoporous Mater.*, 2008, **115**, 215–233.
- 9 E. Sjöberg, L. Sandström, O. G. W. Öhrman and J. Hedlund, *J. Membr. Sci.*, 2013, **443**, 131–137.
- 10 K. V. Agrawal, B. Topuz, T. C. T. Pham, T. H. Nguyen, N. Sauer, N. Rangnekar, H. Zhang, K. Narasimharao, S. N. Basahel, L. F. Francis, C. W. Macosko, S. Al-Thabaiti, M. Tsapatsis and K. B. Yoon, *Adv. Mater.*, 2015, **27**, 3243–3249.
- 11 J. Caro, M. Noack and E. Stefan, in *Advances in Nanoporous Materials*, Elsevier, 2010, vol. 1, pp. 1–96.
- 12 International Zeolite Association (IZA), <http://www.iza-online.org/>.
- 13 L. Sandström, E. Sjöberg and J. Hedlund, *J. Membr. Sci.*, 2011, **380**, 232–240.
- 14 Z. P. Lai, G. Bonilla, I. Diaz, J. G. Nery, K. Sujaoti, M. A. Amat, E. Kokkoli, O. Terasaki, R. W. Thompson, M. Tsapatsis and D. G. Vlachos, *Science*, 2003, **300**, 456–460.
- 15 P. D. Kolokathis, E. Pantatosaki, C.-A. Gatsiou, H. Jobic, G. K. Papadopoulos and D. N. Theodorou, *Mol. Simul.*, 2014, **40**, 80–100.
- 16 J. Kärger, *J. Phys. Chem.*, 1991, **95**, 5558–5560.
- 17 Z. Lai and M. Tsapatsis, *Ind. Eng. Chem. Res.*, 2004, **43**, 3000–3007.
- 18 M. Zhou, D. Korelskiy, P. Ye, M. Grahn and J. Hedlund, *Angew. Chem., Int. Ed.*, 2014, **53**, 3492–3495.
- 19 J. Hedlund, D. Korelskiy, L. Sandström and J. Lindmark, *J. Membr. Sci.*, 2009, **345**, 276–287.
- 20 D. Korelskiy, M. Grahn, J. Mouzon and J. Hedlund, *J. Membr. Sci.*, 2012, **417–418**, 183–192.
- 21 D. Korelskiy, T. Leppäjärvi, H. Zhou, M. Grahn, J. Tanskanen and J. Hedlund, *J. Membr. Sci.*, 2013, **427**, 381–389.
- 22 L. Yu, D. Korelskiy, M. Grahn and J. Hedlund, *Sep. Purif. Technol.*, 2015, **153**, 138–145.
- 23 P. Ye, M. Grahn, D. Korelskiy and J. Hedlund, *AIChE J.*, 2016, **62**, 2833–2842.
- 24 M. Grahn and J. Hedlund, *J. Membr. Sci.*, 2014, **471**, 328–337.
- 25 I. Perdana, B. W. Tyoso, I. M. Bendiyasa, Rochmadi, S. K. Wirawan and D. Creaser, *Chem. Eng. Res. Des.*, 2009, **87**, 1438–1447.
- 26 F. T. de Bruijn, L. Sun, Z. Olujic, P. J. Jansens and F. Kapteijn, *J. Membr. Sci.*, 2003, **223**, 141–156.
- 27 F. Jareman, J. Hedlund, D. Creaser and J. Sterte, *J. Membr. Sci.*, 2004, **236**, 81–89.
- 28 S. Thomas, R. Schäfer, J. Caro and A. Seidel-Morgenstern, *Catal. Today*, 2001, **67**, 205–216.
- 29 R. W. Johnson, *The handbook of fluid dynamics*, CRC Press, Boca Raton, Fla, 1998.
- 30 A. L. Myers and J. M. Prausnitz, *AIChE J.*, 1965, **11**, 121–127.
- 31 L. Ohlin, P. Bazin, F. Thibault-Starzyk, J. Hedlund and M. Grahn, *J. Phys. Chem. C*, 2013, **117**, 16972–16982.
- 32 S. K. Wirawan, M. Petersson and D. Creaser, *ASEAN Journal of Chemical Engineering*, 2008, **8**, 9–19.
- 33 R. Krishna and J. M. van Baten, *J. Membr. Sci.*, 2011, **383**, 289–300.
- 34 R. Krishna, *Microporous Mesoporous Mater.*, 2014, **185**, 30–50.
- 35 G. Zeng, C. Chen, D. Li, B. Hou and Y. Sun, *CrystEngComm*, 2013, **15**, 3521–3524.
- 36 J. Hedlund, F. Jareman, A. J. Bons and M. Anthonis, *J. Membr. Sci.*, 2003, **222**, 163–179.
- 37 W. J. W. Bakker, L. J. P. Van Den Broeke, F. Kapteijn and J. A. Moulijn, *AIChE J.*, 1997, **43**, 2203–2214.
- 38 J. Kärger, H. Pfeifer, F. Stallmach, N. N. Feoktistova and S. P. Zhdanov, *Zeolites*, 1993, **13**, 50–55.
- 39 R. Krishna and J. M. van Baten, *J. Membr. Sci.*, 2010, **360**, 323–333.

